Electronic Supplemental Information for

Steering Electron Transport Properties of Pyridine-Functionalized Fullerene Derivatives in Inverted Perovskite Solar Cells: The Nitrogen Site Matters

Bairu Li,[a] Jieming Zhen,[a] Yangyang Wan,[a] Xunyong Lei,[b] Lingbo Jia,[a] Xiaojun Wu,[a] Hualing Zeng,[b] Muqing Chen,[a] Guan-Wu Wang,*[c] and Shangfeng Yang*[a]*

[a]Hefei National Laboratory for Physical Sciences at Microscale,
CAS Key Laboratory of Materials for Energy Conversion,
Department of Materials Science and Engineering,
Synergetic Innovation Center of Quantum Information & Quantum Physics,
University of Science and Technology of China,
Hefei 230026, China
E-mail: mqchen@ustc.edu.cn; sfyang@ustc.edu.cn

[b]ICQD, Hefei National Laboratory for Physical Sciences at Microscale, CAS Key Laboratory of Strongly-coupled Quantum Matter Physics, University of Science and Technology of China (USTC), Hefei 230026, China

[c]CAS Key Laboratory of Soft Matter Chemistry,
Hefei National Laboratory for Physical Sciences at Microscale,
Collaborative Innovation Center of Chemistry for Energy Materials (iChEM),
Department of Chemistry,
University of Science and Technology of China,
Hefei 230026, China
E-mail: gwang@ustc.edu.cn

Contents

S1. MALDI-TOF mass spectra of C_{60}-n-Py (n=2, 3, 4).

S2. ^{1}H NMR and ^{13}C NMR spectra of C_{60}-n-Py (n=2, 3, 4).

S3. FTIR spectra of C_{60}-n-Py (n=2, 3, 4).

S4. Crystal parameters of C_{60}-n-Py (n=2, 3, 4) obtained by X-ray single crystal diffraction.

S5. TGA analysis of C_{60}-n-Py (n=2, 3, 4).

S6. Estimation of the energy levels of C_{60}-n-Py (n=2, 3, 4) and PCBM.

S7. Photovoltaic parameters of devices using different C_{60}-n-Py (n=2, 3, 4). as ETL deposited with the same procedure.

S8. Optimization of the film thickness of C_{60}-3-Py, C_{60}-4-Py ETL.

S9. Statistic photovoltaic parameters for the C_{60}-n-Py (n=2, 3, 4) and PCBM-based devices.

S10. Photovoltaic parameters of devices with C_{60}-n-Py (n=2, 3, 4) ETLs in different scan direction.

S11. AFM height images of perovskite films modified by C_{60}-n-Py (n=2, 3, 4) and PCBM.

S12. Analysis of time-resolved photoluminescence (TRPL) spectra of the perovskite film with C_{60}-n-Py (n=2, 3, 4) and PCBM ETLs.

S13. Trap state densities of perovskite films with C_{60}-n-Py (n=2, 3, 4) and PCBM ETLs measured by SCLC method.

S14. Electron mobility of $CH_3NH_3PbI_3$ films with C_{60}-n-Py (n=2, 3, 4) and PCBM ETLs estimated by SCLC method.

S15. Parameters employed for the fitting of the impedance spectra.

S16. Stabilized photocurrent density and power output of the C_{60}-n-Py-based (n=2, 3, 4) devices.

S17. Wettabilities of C_{60}-n-Py (n=2, 3, 4) films.

S18. Device fabrication procedure and photovoltaic parameters of the $Cs_{0.05}FA_{0.83}MA_{0.12}PbI_{2.55}Br_{0.45}$ iPSCs with C_{60}-n-Py (n=2, 3, 4) and PCBM ETLs

***S1. MALDI-TOF mass spectra of C_{60}-n-Py* (n=2, 3, 4).**

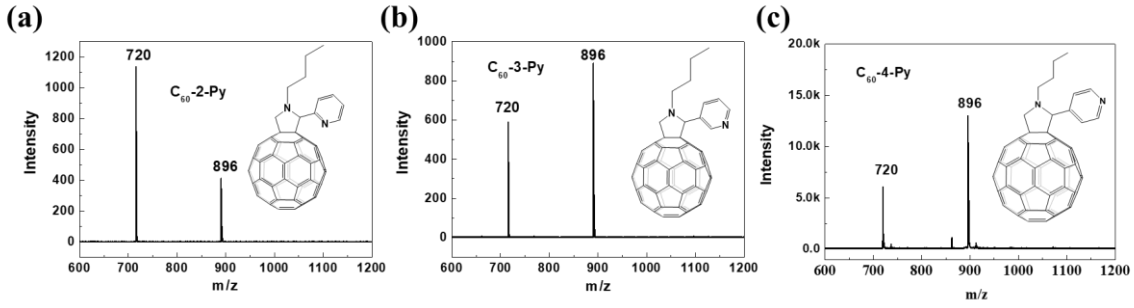

Figure S1. MALDI-TOF Mass spectra of (a) C_{60}-2-Py, (b) C_{60}-3-Py, (c) C_{60}-4-Py. (The MALDI-TOF Mass spectra of C_{60}-4-Py is Cited from the reference S1 we reported previously.)

***S2. ^{1}H NMR and ^{13}C NMR spectra of C_{60}-n-Py* (n=2, 3, 4).**

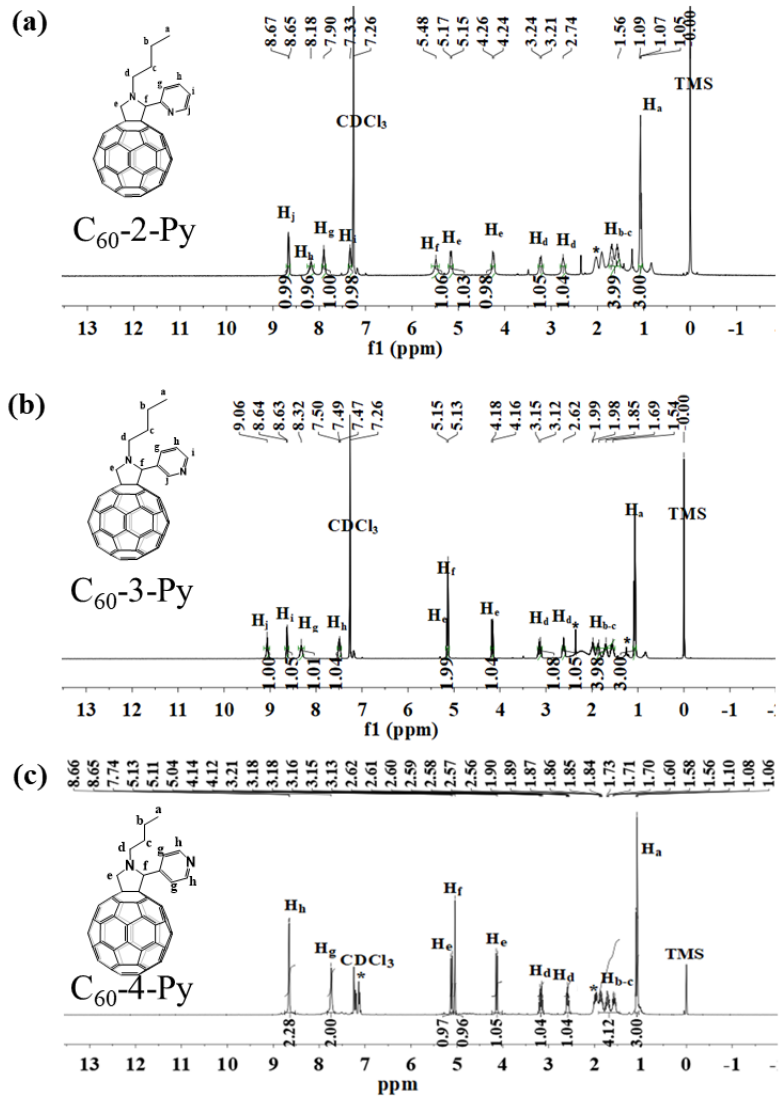

Figure S2. ^{1}H NMR spectra of (a) C_{60}-2-Py, (b) C_{60}-3-Py, (c) C_{60}-4-Py. (The ^{1}H NMR spectra of C_{60}-4-Py is Cited from the reference S1 we reported previously.)

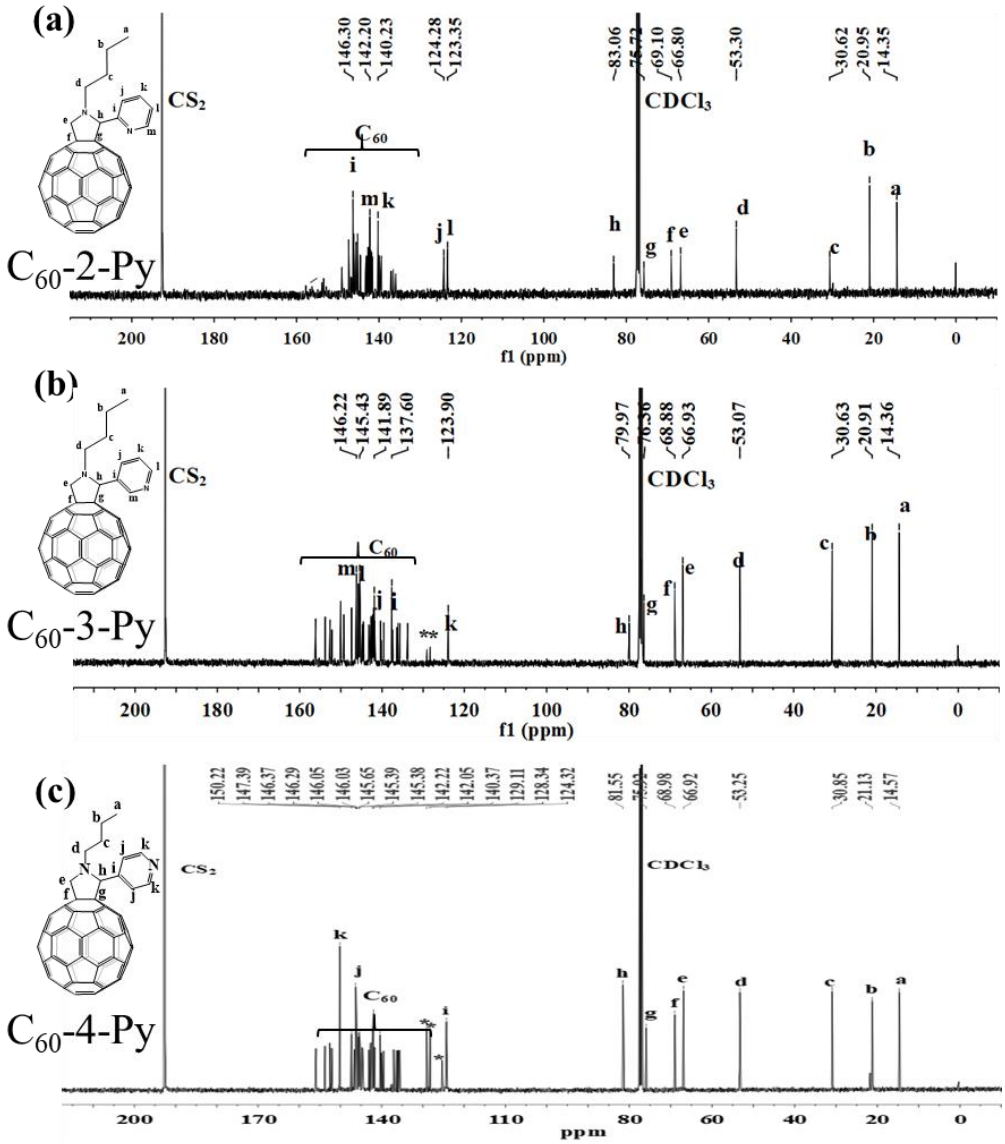

Figure S3. ^{13}C NMR spectra of (a) C_{60}-2-Py, (b) C_{60}-3-Py, (c) C_{60}-4-Py in $CS_2/CDCl_3$, the peaks at (192.5 ppm) and (77 - 77.7 ppm) represent the signals of solvents of CS_2 and $CDCl_3$. (^{13}C NMR spectra of C_{60}-4-Py is Cited from the reference S1 we reported previously.)

***S3. FTIR spectra of C_{60}-n-Py* (n=2, 3, 4).**

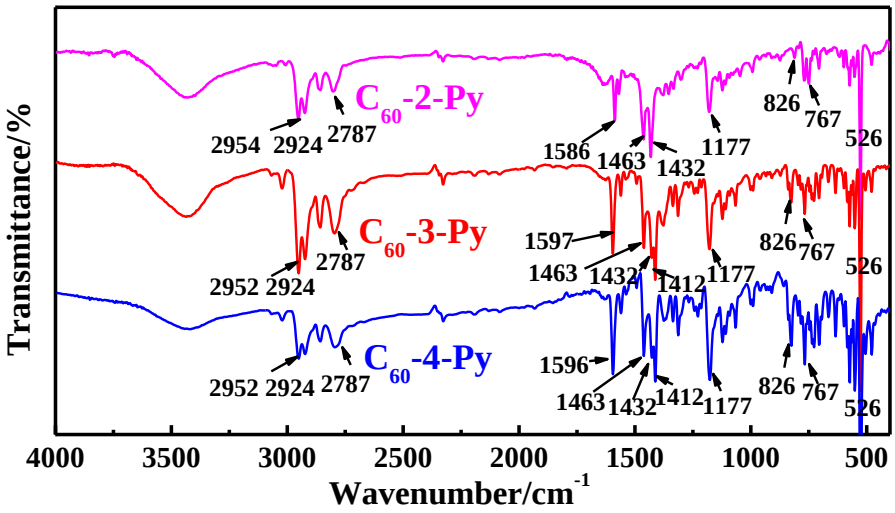

Figure S4. FTIR spectra of (a) C_{60}-2-Py, (b) C_{60}-3-Py and (c) C_{60}-4-Py.

S4. Crystal parameters of C_{60}-n-Py (n=2, 3, 4) obtained by X-ray single crystal diffraction.

Table S1 The crystal parameters of C_{60}-n-Py (n=2, 3, 4)

Crystal	C_{60}-2-Py	C_{60}-3-Py	C_{60}-4-Py
Formula	C192H94.7N21	C198H102N22	C191H95.06N22
Formula weight	2695.58	2789.01	2698.51
Color, habit	Black, block	Black, block	Black, block
Crystal system	monoclinic	monoclinic	monoclinic
Space group	*P21/c*	*P21/c*	*P21/c*
a, Å	14.316	30.750	14.3847(9)
b, Å	32.479	27.543	32.4491(19)
c, Å	28.389	18.176	28.3555(17)
α, deg	90	90	90
β, deg	93.72	98.29	93.508(2)
γ, deg	90	90	90
Volume, Å^3	13172.2	15233.1	13210.7(14)
Z	4	4	4
T, K	173(2)	173(2)	173(2)
Radiation (λ, Å)	synchrotron (λ = 0.71073)	synchrotron (λ = 0.71073)	synchrotron (λ = 0.71073)
Unique data (Rint)	24647(0.135)	16807(0.109)	26894(0.0901)
Parameters	2460	2036	2478
Restraints	1554	1944	2103
Observed data (I > 2σ(I))	24647	16807	175410
R1[a] (observed data)	0.0967	0.1137	0.1500
wR2[b] (all data)	0.2730	0.2791	0.3818

Table S2 The distances of carbon cage-carbon cage and pyridine nitrogen sites-carbon cage

Crystal	C_{60}-2-Py	C_{60}-3-Py	C_{60}-4-Py
Distance of carbon cage and carbon cage	10.037	11.298	10.334
	7.368	9.052	7.292
	-	9.728	-
Distance of cage and pyridine nitrogen sites	8.947	7.165	11.919

***S5. TGA analysis of C_{60}-n-Py* (n=2, 3, 4).**

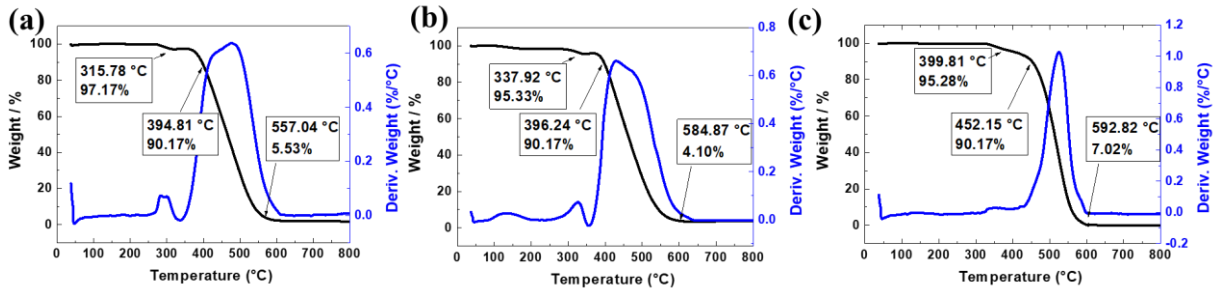

Figure S5. TGA curves (black lines) and differential thermo-gravimetric (DTG) curve (blue lines) of (a) C_{60}-2-Py, (b) C_{60}-3-Py, (c) C_{60}-4-Py

According to the TGA curves of C_{60}-n-Py, the decomposition temperature of the first weight-loss step, which correlates to the detachment of the functional groups of C_{60}-n-Py, are 394.81 ^{o}C, 396.24 ^{o}C and 452.15 ^{o}C for C_{60}-2-BPy, C_{60}-3-BPy and C_{60}-4-BPy, respectively, indicating the detachment of functional groups in fullerene derivatives. The second weight-loss step is related to the decomposition of C_{60} cage within pyridine-functionalized fullerene derivatives and the corresponding decomposition temperatures are 557.04 ^{o}C, 584.87 ^{o}C, 592.82 ^{o}C, respectively. Such high decomposition temperatures of C_{60}-n-BPy ensure their considerable thermal stabilities, fullfilling the requirments of iPSC device fabrication.

S6. Estimation of the energy levels of C_{60}-n-Py* (n=2, 3, 4) *and PCBM.

Table S3. Electrochemical data of C_{60}-n-Py (n=2, 3, 4) and PCBM.

	λ_{onset} [a] (nm)	$E_{g,opt}$ [b] (eV)	$E_{onset,red}$ [c] (eV)	E_{LUMO} [d] (eV)	E_{HOMO} [e] (eV)
PCBM	724	1.71	-0.98	-3.82	-5.53
C_{60}-2-Py	715	1.73	-1.02	-3.78	-5.51
C_{60}-3-Py	724	1.71	-1.00	-3.80	-5.51
C_{60}-4-Py	724	1.71	-0.99	-3.81	-5.52

[a] Attained from UV-vis spectrum; [b] $E_{g,opt}=1240/\lambda_{onset}$; [c] Referred to the half wave potential of ferrocene;

[d] $E_{LUMO}=-e(E_{onset,\ red}+4.8\ V)$;[e] $E_{HOMO}=E_{LUMO}-E_{g,opt}$.

The energy levels of the lowest unoccupied molecular orbital (LUMO) and highest occupied molecular orbital (HOMO) of the fullerene derivatives were estimated by a cyclic voltammetry study in combination with UV-Vis absorption spectroscopy. Cyclic voltammetry study was performed in *o*-dichlorobenzene with a CHI 630D potentiostat (CHI Instrument, U.S.A.) at room temperature. Tetrabutylammonium perchlorate (TBPA, electrochemical grade, Fluka) was used as the supporting electrolyte was. A standard three-electrode arrangement of a platinum (Pt) wire as counter electrode, a platinum coil as working electrode, and a saturated calomel electrode as a pseudo-reference electrode was used. In a comparison experiment, ferrocene (Fc) was added as the internal standard and all potentials are referred to the Fc^+/Fc couple.

The onset reduction potentials (E_{red}^{onset}) of C_{60}-2-Py, C_{60}-3-Py, C_{60}-4-Py and PCBM were estimated to be -1.02, -1.00, -0.99 and -0.98 V vs Fc^+/Fc, respectively. Hence, the LUMO energy levels of C_{60}-2-Py, C_{60}-3-Py, C_{60}-4-Py and PCBM are -5.51, -5.51, -5.52 and -5.53 eV calculated by $E_{LUMO}= -e(E_{red}^{onset} + 4.8)$, respectively. The HOMO energy level of C_{60}-2-Py, C_{60}-3-Py, C_{60}-4-Py and PCBM are calculated by $E_{HOMO}=E_g^{opt} - E_{LUMO}$,[S2, S3] where E_g^{opt} is the optical bandgap. Based on the onset (λ_{onset}) of UV-vis absorption spectrum of C_{60}-2-Py, C_{60}-3-Py, C_{60}-4-Py and PCBM (~715, ~724, ~724, ~724 nm, see Fig. 1b.), E_g^{opt} is estimated to be ~ 1.73, 1.71, 1.71 and 1.71 eV, respectively, according to the equation: $E_g^{opt} = 1240/\lambda_{onset}$.[S4, S5] A small blue shift of λ_{onset} is observed for C_{60}-2-Py, which is likely due to the different intramolecular charge transfer between C_{60} cage and the pyridine moiety. However, such a small blue shift of λ_{onset} results in only negligible influence on the E_g^{opt}. Accordingly, the HOMO energy levels of C_{60}-2-Py, C_{60}-3-Py, C_{60}-4-Py and PCBM are estimated to be -5.51, -5.51, -5.52 and -5.53 eV, respectively.

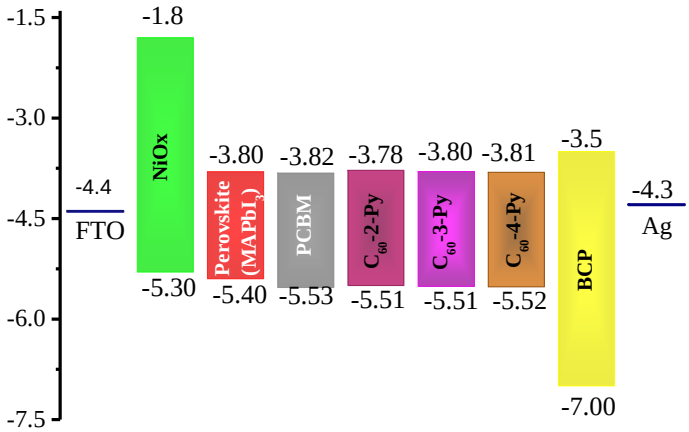

Figure S6. The energy level diagram of the materials used in the perovskite solar cells

S7. Photovoltaic parameters of devices using different C_{60}-n-Py (n=2, 3, 4) as ETL deposited with the same procedure.

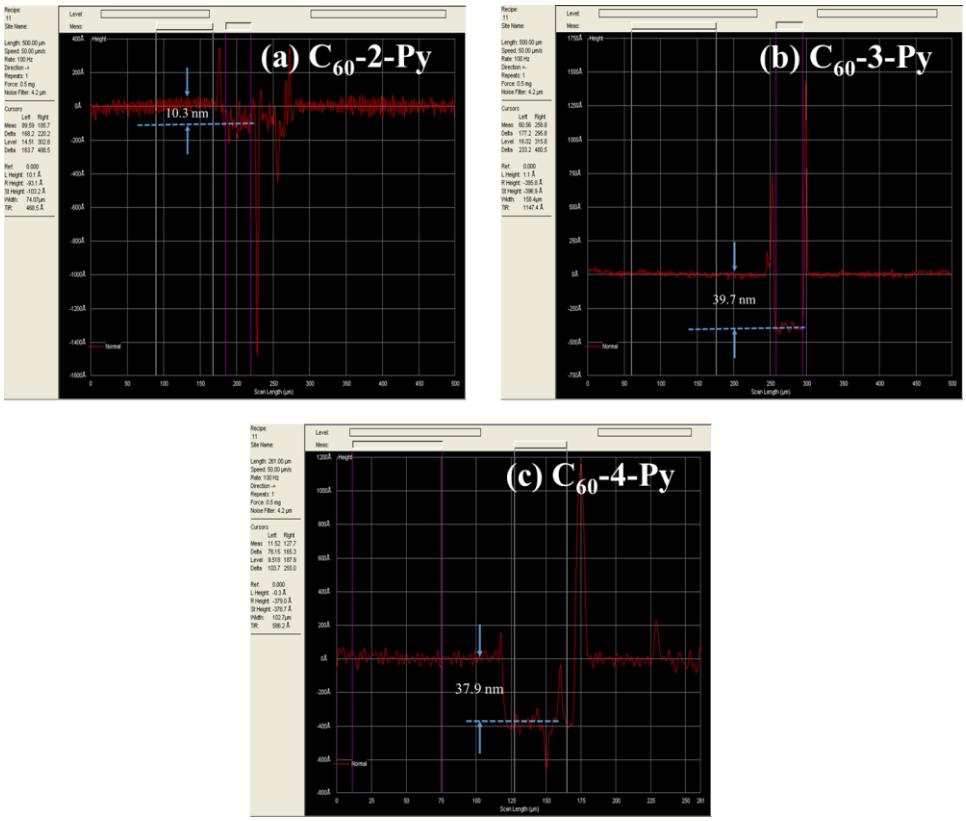

Figure S7. Figure S7 Surface profiles of (a) C_{60}-2-Py, (b) C_{60}-3-Py (c) C_{60}-4-Py ETLs measured on KLA-Tencor P6 surface profilometer under the optimized solution concentration and pin-coating speed.

Table S4. Photovoltaic parameters of devices with different C_{60}-n-Py (n=2, 3, 4) ETLs deposited at the same concentration (9 mg/ml in CB) and the same spin-coating speed. The parameters were averaged by over 10 devices fabricated independently.

ETL	Spin-coating speed	V_{oc} (V)	J_{sc} (mA/cm^2)	FF (%)	PCE (%)	R_s (Ω·cm^2)	R_{sh} (Ω·cm^2)
C_{60}-2-Py	1000 rpm	0.97±0.03	18.24±1.99	56.76±4.87	10.01±1.72	9.1	807.5
	3000 rpm	0.92±0.01	13.67±1.01	51.03±3.24	6.44±0.86	13.8	460.2
C_{60}-3-Py	1000 rpm	0.97±0.01	22.07±0.72	66.12±0.83	14.20±0.41	5.5	1541.4
	3000 rpm	0.98±0.02	21.43±0.94	56.77±2.81	12.00±1.06	7.3	1419.0
C_{60}-4-Py	1000 rpm	0.97±0.02	21.30±1.05	64.25±0.65	13.29±0.72	6.1	1483.3
	3000 rpm	0.95±0.01	20.23±2.42	53.94±3.79	10.41±1.98	8.4	857.4

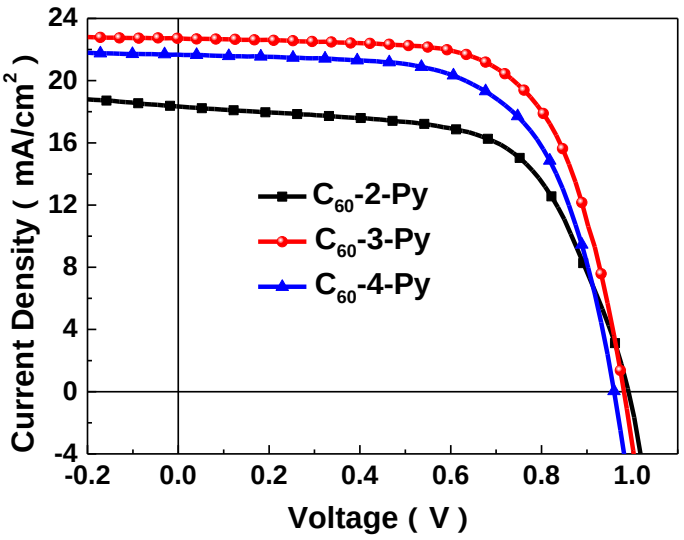

Figure S8. The J-V curves of the devices with C_{60}-2-Py, C_{60}-3-Py, and C_{60}-4-py as electron transport layers (ETLs) deposited at the same concentration (9 mg/ml in CB) and the same spin-coating speed. The scanning direction is from open-circuit voltage to short circuit (reverse).

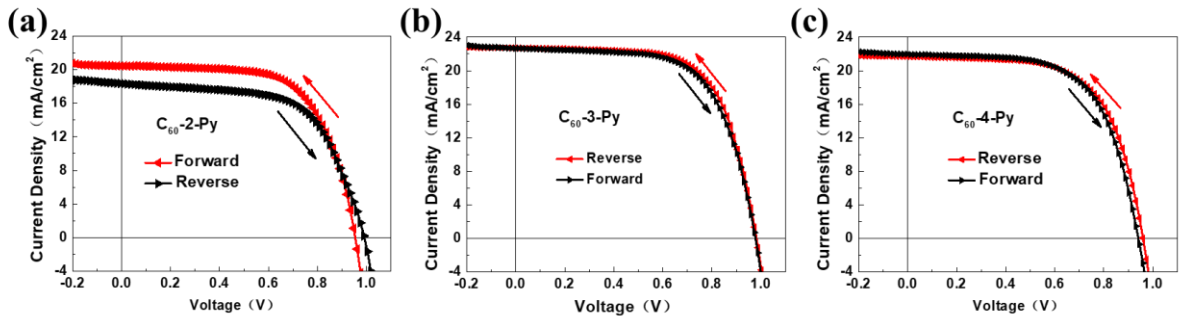

Figure S9. The J-V curves of the best performance devices using (a) C_{60}-2-Py, (b) C_{60}-3-Py and (c) C_{60}-4-Py (9 mg/ml in CB, spin-coating speed 1000rpm) as ETLs in different scan direction. Inset shows the photovoltaic parameters and hysteresis index.

Table S5. Photovoltaic parameters and hysteresis index of the best performance devices using (a) C_{60}-2-Py, (b) C_{60}-3-Py and (c) C_{60}-4-Py (9 mg/ml in CB, spin-coating speed 1000rpm) as electron transporting layers in different scan direction.

ETL	Scanning direction	V_{oc} (V)	J_{sc} (mA/cm^2)	FF(%)	PCE(%)	Hysteresis index[a] (%)
C_{60}-2-Py	Reverse	0.95	20.45	64.67	12.68	10.65
	Forward	0.99	18.36	62.41	11.33	
C_{60}-3-Py	Reverse	0.98	22.70	66.38	14.78	2.71
	Forward	0.98	22.70	64.84	14.38	
C_{60}-4-Py	Reverse	0.96	21.66	63.84	13.27	6.41
	Forward	0.96	21.88	59.22	12.42	

[a] Hystersis index = [PCE(reverse) - PCE(forward)]/PCE(reverse)

S8. Optimization of the film thickness of C_{60}-3-Py, C_{60}-4-Py ETL.

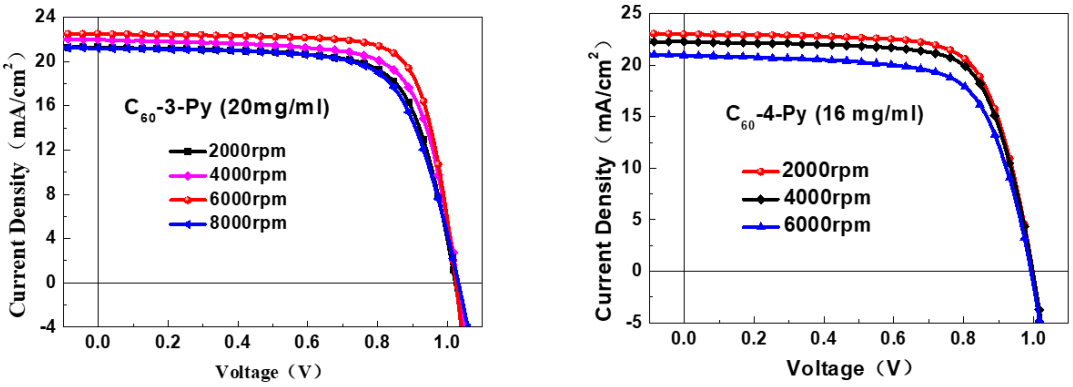

Figure S10. J-V curves of (a) C_{60}-3-Py, (b) C_{60}-4-Py-based devices produced by different spin-coating speed with certain concentrations in chlorobenzene.

Table S6. Photovoltaic parameters of devices with different C_{60}-n-Py (n=2, 3, 4) ETLs deposited by different spin-coating rate. The parameters were averaged by over 5 devices fabricated independently.

ETL	concentration	Spin-coating speed	V_{oc} (V)	J_{sc} (mA/cm^2)	FF(%)	PCE(%)
C_{60}-2-Py	9 mg/ml	1000rpm	0.97±0.03	18.24±1.99	56.76±4.87	10.01±1.72
		3000rpm	0.92±0.01	13.67±1.01	51.03±3.24	6.44±0.86
C_{60}-3-Py	20 mg/ml	2000rpm	1.00±0.01	21.09±0.84	71.35±1.40	15.07±0.43
		4000rpm	1.02±0.01	21.39±0.58	73.24±1.45	15.96±0.80
		6000rpm	1.02±0.01	21.99±0.92	74.33±1.64	16.73±0.60
		8000rpm	1.00±0.01	21.68±0.58	68.76±0.77	14.81±0.46
C_{60}-4-Py	16 mg/ml	2000rpm	1.00±0.004	21.59±0.54	73.02±0.57	15.57±0.46
		4000rpm	1.00±0.001	21.18±0.74	71.12±1.76	15.53±0.84
		6000rpm	1.00±0.016	19.76±0.42	69.34±2.68	13.66±0.36

S9. Statistic photovoltaic parameters for C_{60}-n-Py (n=2, 3, 4) and PCBM-based devices.

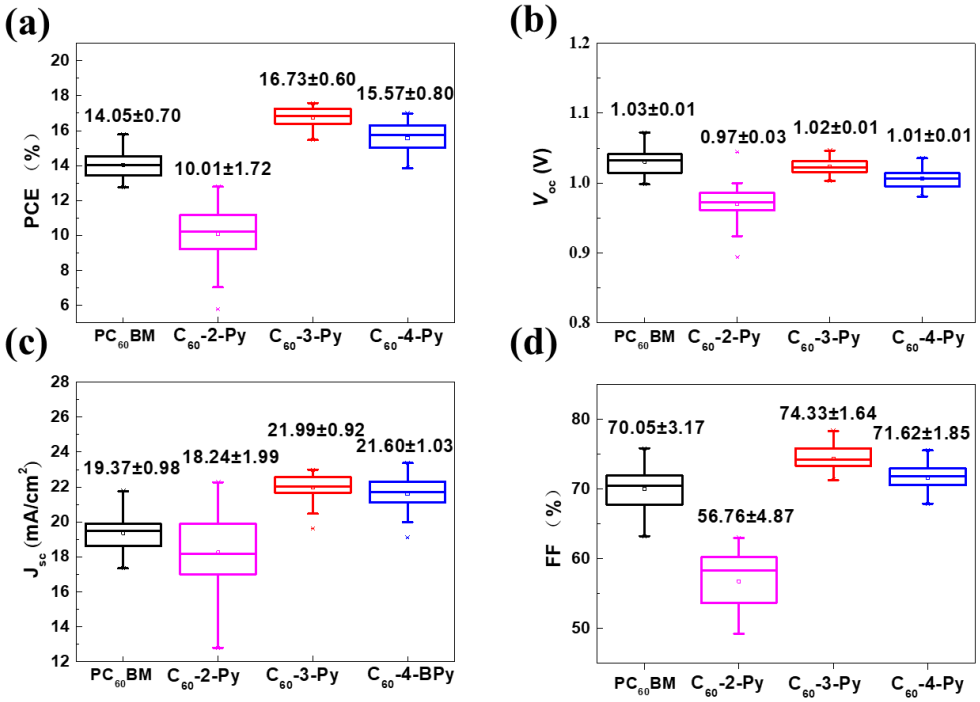

Figure S11. Box plots of PCE (a), V_{oc} (b), J_{sc} (c) and FF (d) for the PCBM and C_{60}-n-Py based devices.

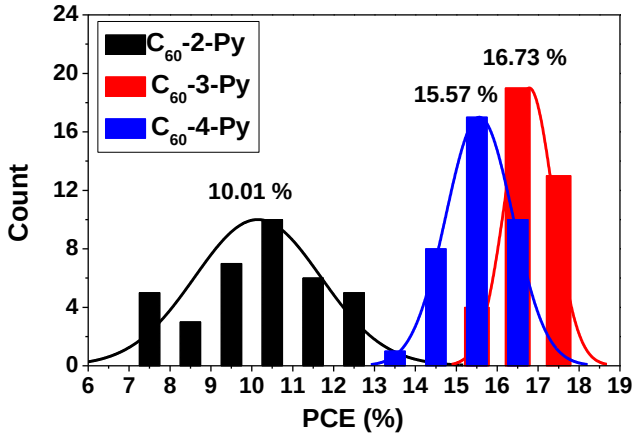

Figure S12. PCE histograms of the C_{60}-n-Py (n=2, 3, 4)-based devices.

S10. Photovoltaic parameters of devices with fullerene derivative ETLs in different scan directions.

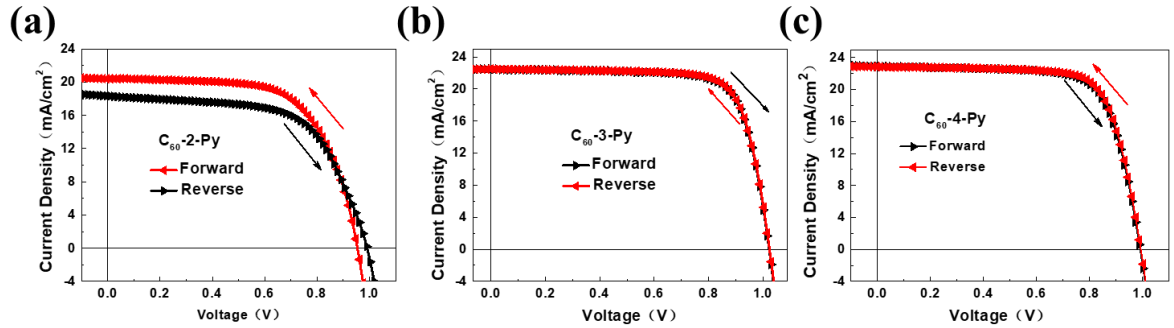

Figure S13. The J-V curves of the best performance devices using different fullerene derivative, (a) C_{60}-2-Py, (b) C_{60}-3-Py, (c) C_{60}-4-Py as ETLs in different scan direction.

Table S7. Photovoltaic parameters of of best performance devices using C_{60}-2-Py, C_{60}-3-Py and C_{60}-4-Py as ETLs under forward and reverse scans.

ETL	Scanning direction	V_{oc} (V)	J_{sc} (mA/cm^2)	FF(%)	PCE(%)	Hysteresis index[a] (%)
C_{60}-2-Py	Reverse	0.95	20.45	64.67	12.68	10.65
	Forward	0.99	18.36	62.41	11.33	
C_{60}-3-Py	Reverse	1.02	22.46	76.42	17.57	0.46
	Forward	1.02	22.47	76.20	17.49	
C_{60}-4-Py	Reverse	1.00	22.85	74.20	16.83	1.37
	Forward	1.00	22.93	73.09	16.60	

[a] Hystersis index = [PCE(reverse) - PCE(forward)]/PCE(reverse)

S11. AFM height images of perovskite films modified by C_{60}-n-Py (n-2, 3, 4) and PCBM.

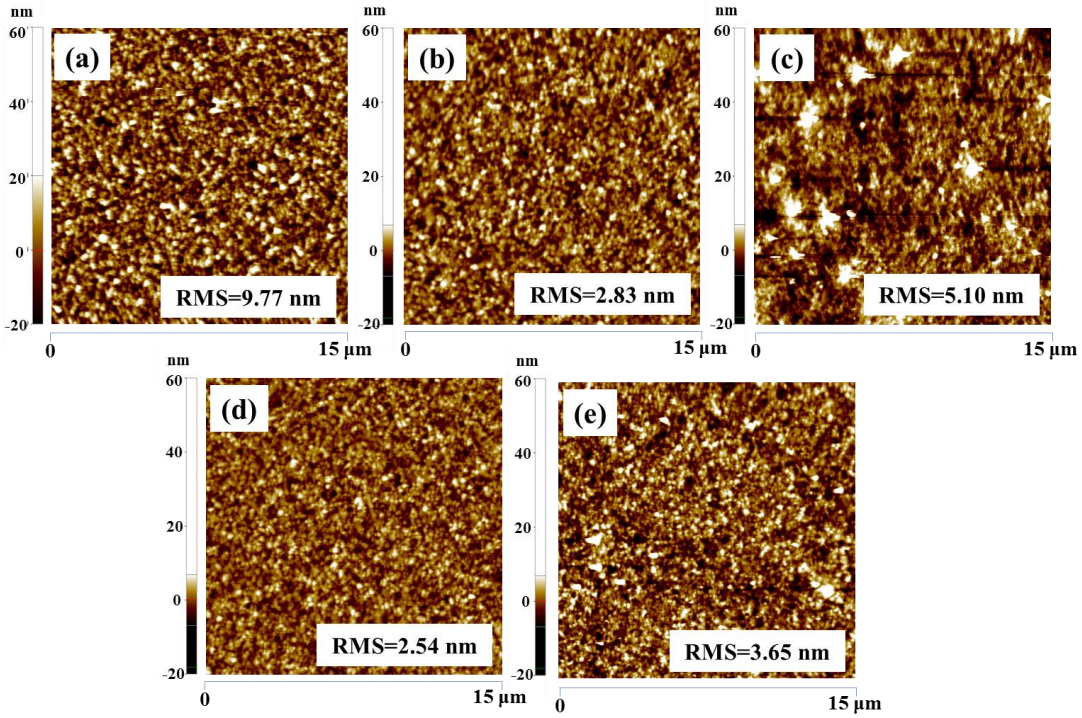

Figure S14. AFM height images (15μm × 15μm) of (a) FTO/NiO_x/$CH_3NH_3PbI_3$, (b) FTO/NiO_x/$CH_3NH_3PbI_3$/PCBM, (c) FTO/NiO_x/$CH_3NH_3PbI_3$/C_{60}-2-Py, (d) FTO/NiO_x/$CH_3NH_3PbI_3$/C_{60}-3-Py,(e) FTO/NiO_x/$CH_3NH_3PbI_3$/C_{60}-4-Py films.

S12. Analysis of time-resolved photoluminescence (TRPL) spectra of the perovskite film with C_{60}-n-Py* (n=2, 3, 4) *and PCBM ETLs.

To further explored the charge recombination dynamics, TRPL spectra of perovskite film w/o C_{60}-n-Py (n=2, 3, 4) and PCBM as ETLs are measured (Figure 4b). The lifetime was obtained by fitting the TRPL spectra by a bi-exponential decay function as shown in equation S1.[S6-S8]

$$F(t)=A_1 \exp(-t/\tau_1)+A_2\exp(-t-t/\tau_2)+y_0 \quad \text{(S1)}$$

Where A1 and A2 are the decay amplitude, the decay lifetime τ1 and τ2 are the fast and slow decay time, y_0 is a constant for the basline offset, respectively. The fast decay is considered to be the reults of quenching of free charges in perovskite film through transport to the elcctron transport layers, while the slow decay is to be the result of nonradiative recombination of trapped charges within $CH_3NH_3PbI_3$ perovskite film. We calculated the average decay time (τ_{ave}) according to the formula $\tau_{ave} = (A_1\tau_1^2+ A_2\tau_2^2)/ (A_1\tau_1+ A_2\tau_2)$. The pristine $CH_3NH_3PbI_3$ perovskite film shows a τ_{ave} of 22.63 ns. The C_{60}-2-Py, C_{60}-3-Py, C_{60}-4-Py and PCBM based films show average lifetime of 18.17 ns, 9.16 ns, 4.63 ns and 7.91 ns respectively, which demonstrated that C_{60}-3-Py are the most efficient electron acceptor for $CH_3NH_3PbI_3$ perovskite film.

S13. Trap state densities of perovskite films with C_{60}-n-Py* (n=2, 3, 4) *and PCBM ETLs measured by SCLC method.

Electron-only devices with a structure of ITO/TiO_2/perovskite/ETL/Ag was fabricated to measure the trap state density of $CH_3NH_3PbI_3$ perovskite film deposited with different C_{60}-n-Py (n=2, 3, 4) and PCBM. The J-V curves of these devices measured under dark condition are shown in Figure 4c. As can be seen, an ohmic response is emerged at the low bias, where the J-V curve exhibits linear $V\propto$correlation. With bias voltage increases, the current increases nonlinearly, which indexes as trap-filled limit region ($I \propto V^{n>3}$). The kink point between ohmic regime and trap-filled limit region is defined as the trap-filled limit voltage (V_{TFL}). Trap-state density (n_t) can be determined through equation as follow:

$$n_t = \frac{2\varepsilon\varepsilon_0}{eL^2} \cdot V_{TFL} \quad \text{(S2)}$$

Where ε is the relative dielectric constant of $CH_3NH_3PbI_3$ (28.8), ε_0 is the vacuum permittivity (ε_0 = 8.854 ×10^{-12} F/m), e is the elementary charge of the electron (e = 1.6 ×10^{-19} C), and L is the perovskite film thickness(~300nm). The V_{TFL} of the $CH_3NH_3PbI_3$ perovskite films after deposited with C_{60}-2-Py, C_{60}-3-Py C_{60}-4-Py and PCBM are 0.831 V, 0.589 V, 0.633 V and 0.769 V, corresponding to n_t of 2.946×10^{16} cm^{-3}, 2.088×10^{16} cm^{-3}, 2.243×10^{16} and 2.762×10^{16} cm^{-3}.

S14. Electron mobilities of $CH_3NH_3PbI_3$ films with C_{60}-n-Py (n=2, 3, 4) and PCBM ETLs estimated by SCLC method.

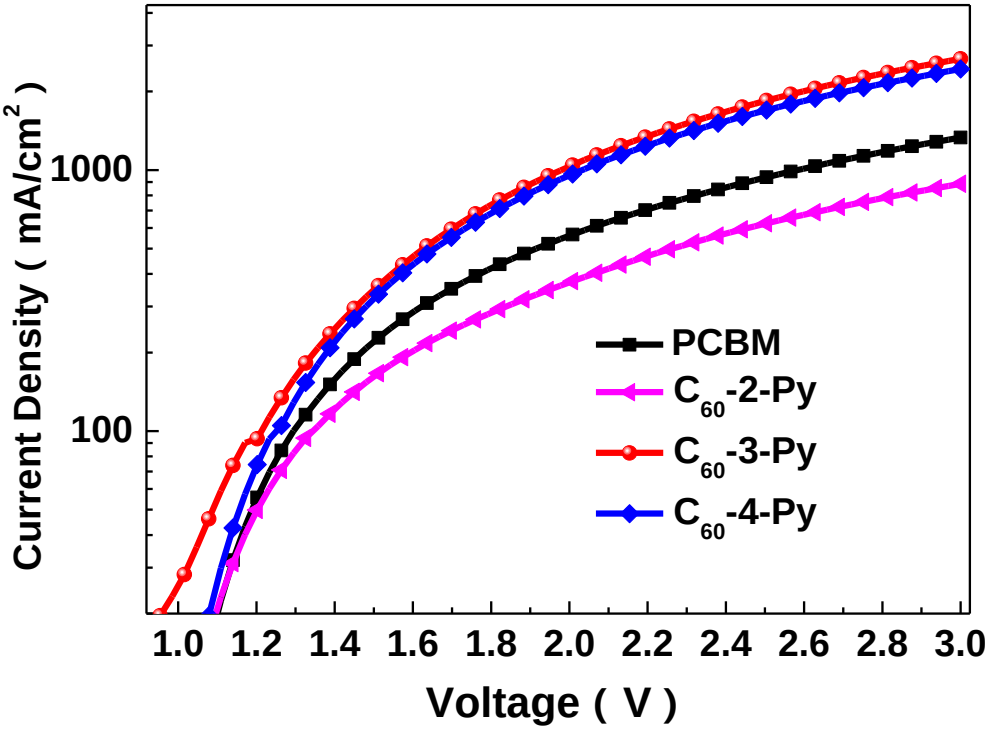

Figure S15. Current-voltage data from the electron-only devices using C_{60}-n-Py (n=2, 3, 4) and PCBM as ETL. The device architecture is ITO/ $CH_3NH_3PbI_3$/ETL/Ag.

The electron mobility of $CH_3NH_3PbI_3$ films with different fullerene derivatives is estimated by SCLC method. The μ value is calculated from the Mott–Gurney equation:

$$J_d = \frac{9\varepsilon\varepsilon_0}{8L^3} \cdot V^2 \cdot \mu \qquad \text{(S3)}$$

Where the J_d is current density and μ is carrier mobility, L is the thickness of the $CH_3NH_3PbI_3$ film (300 nm). According to equation (S3), the electron mobility of C_{60}-2-Py, C_{60}-3-Py C_{60}-4-Py and PCBM based device is 1.02×10^{-3} $cm^2V^{-1}S^{-1}$, 2.95×10^{-3} $cm^2V^{-1}S^{-1}$ and 2.64×10^{-3} $cm^2V^{-1}S^{-1}$, 1.44×10^{-4} $cm^2V^{-1}S^{-1}$.

S15. Parameters employed for the fitting of impedance spectra.

From the Nyquist plot (Figure 4d), we fitted the imedance spectras with one R-CPE arcs, which a resistor R_s (series resistance) and parallel with an R-CPE elements. R_s is determined by the starting point at the real part of the Nyquist plot. The R_{ct} (charge transfer resistance) is associated with the charge transfer process at the perovskite/ETL interface, CPE is the non-ideal chemical capacitances.

Table S8. Parameters employed for the fitting of impedance spectra.

ETL	R_s ($\Omega \cdot cm^2$)	R_{ct} ($\Omega \cdot cm^2$)	CPE-T (F/cm^2)	CPE-P
$PC_{61}BM$	19.46	308.5	4.19E-08	0.8931
C_{60}-2-Py	17.84	511.6	7.14E-08	0.8612
C_{60}-3-Py	19.85	53.2	5.45E-08	0.9040
C_{60}-4-Py	16.62	178.5	7.28E-08	0.8829

S16. Stabilized photocurrent density and power output of the C_{60}-n-Py-based* (n=2, 3, 4) *devices.

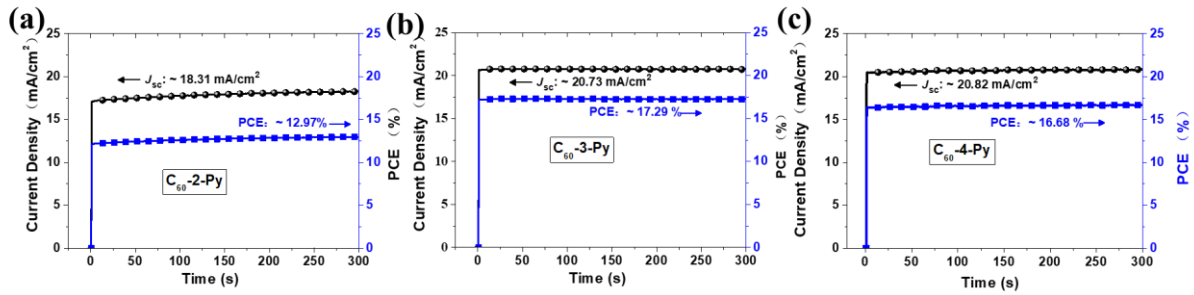

Figure S16. Stabilized photocurrent and power output of devices using (a) C_{60}-2-Py, (b) C_{60}-3-Py, (c) C_{60}-4-Py as ETLs measured at the maximum power points. (0.710 V, 0.832 V and 0.801 V for C_{60}-2-Py-, C_{60}-3-Py- and C_{60}-4-Py-based devices respectively.)

S17. Wettabilities of C_{60}-n-Py (n=2, 3, 4) films.

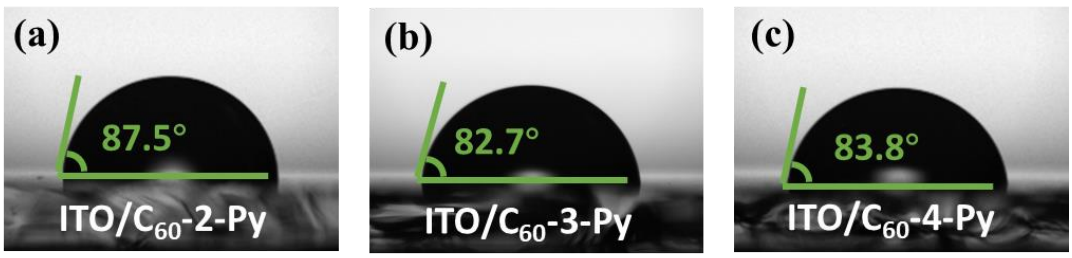

Figure S17. Water contact angles on (a) ITO/C_{60}-2-Py, (b) ITO/C_{60}-3-Py, (c) ITO/C_{60}-4-Py films.

S18. Device fabrication procedure and photovoltaic parameters of the $Cs_{0.05}FA_{0.83}MA_{0.12}PbI_{2.55}Br_{0.45}$ iPSCs with C_{60}-n-Py* (n=2, 3, 4) *and PCBM ETLs

For CsFAMA iPSC devices fabrication, PTAA HTL was spin-coated on the precleaned substrate at 4000 rpm for 30s from a solution of 2mg/ml in toluene. The PTAA film were annealed at 100°C for 10 min. Next, CsFAMA perovskite precursor solution (1.3 M dissolved in DMSO and DMF with a volume ratio of 2:8, with a molar tatios of $PbI_2/PbBr_2$=1.1:0.2, FAI:MABr=1:0.2, CsI/(FAI+MABr)=0.05:0.95, PbI_2/FAI=1.1:1, $PbBr_2$:MABr=1:0.2) was spin-coated onto PTAA HTL with a two-step procedure. The first step was 2000 rpm for 10 s with an acceleration of 200 rpm. The second step was 6000 rpm for 30s with a acceleration of 2000 rpm. At 15 s before the end of the sencond procedure, 100 μL CB was dropped on the spinning substrate. The substrate was then immediately transferred on a hotplate and heated at 100 °C for 60 min. The depositon procedures of ETLs, BCP and Ag electrode are the same as $MAPbI_3$ iPSC devices.

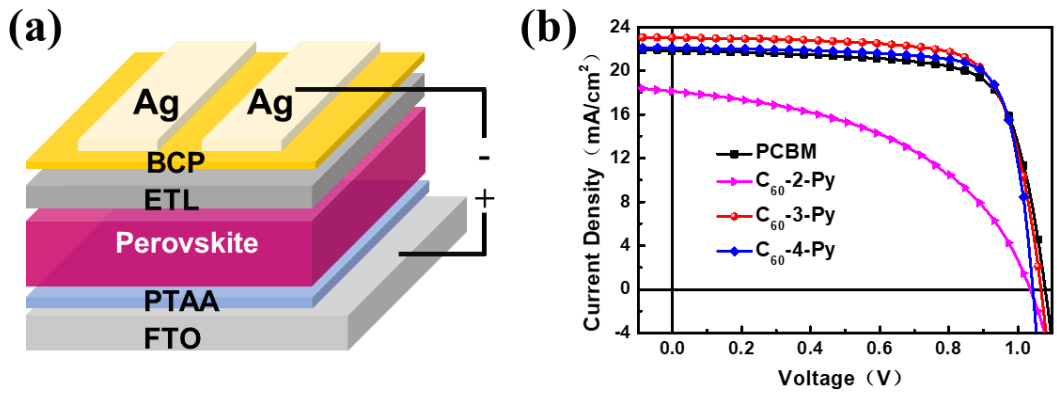

Figure S18. (a) Device structure of the $Cs_{0.05}FA_{0.83}MA_{0.12}PbI_{2.55}Br_{0.45}$ based iPSC with C_{60}-n-Py (n=2, 3, 4) and PCBM as ETLs. (b) J-V curves of the champion device based on defferent ETL measured under illumination of an AM 1.5 solar simulator (100 mW cm^2) in air. The scanning direction is from open-circuit voltage to short circuit (reverse).

Table S9. Photovoltaic parameters of the $Cs_{0.05}FA_{0.83}MA_{0.12}PbI_{2.55}Br_{0.45}$ iPSCs with C_{60}-n-Py (n=2, 3, 4) and PCBM ETLs under one sun illumination (AM 1.5G, 100 mA cm^{-2})

device	ETL	V_{oc} (V)	J_{sc} (mA/cm^2)	FF (%)	PCE (%)		R_s [b]	R_{sh} [b]
					Average[a]	Best	(Ω·cm^2)	(Ω·cm^2)
A	PCBM	1.06±0.02	20.96±0.74	69.42±3.60	15.53±1.27	17.35	5.4	1094.6
B	C_{60}-2-Py	1.05±0.02	18.61±1.73	42.56±5.33	8.44±1.70	10.07	17.4	226.1
C	C_{60}-3-Py	1.05±0.02	22.84±0.63	72.26±2.36	17.32±1.02	18.65	4.4	1945.6
D	C_{60}-4-Py	1.04±0.03	22.10±0.68	71.86±4.25	16.52±1.18	17.91	4.4	1512.9

[a]Averaged over 10 devices fabricated independently. [b] Rs and Rsh are obtained by the PCE measurement system.

Reference

S1 B. Li, J. Zhen, Y. Wan, X. Lei, Q. Liu, Y. Liu, L. Jia, X. Wu, H. Zeng, W. Zhang, G. W. Wang, M. Chen and S. Yang, *ACS Appl. Mater. Interfaces*, 2018, **10**, 32471.

S2 H. Wang, W. Zhang, C. Xu, X. Bi, B. Chen and S. Yang, *ACS Appl. Mater. Interfaces*, 2013**, *5***, 26.

S3 N. Li, C. J. Brabec, *Energy Environ. Sci.*, 2015, ***8***, 2902.

S4 M. Wang, X. Hu, P. Liu, W. Li, X. Gong, F. Huang and Y. Cao, *J. Am. Chem. Soc.*, 2011**, *133***, 9638.

S5 N. Wang, L. Sun, X. Zhang, X. Bao, W. Zheng and R. Yang, *RSC Advances*, 2014**, *4***, 25886.

S6 Y. Lin, L. Shen, J. Dai, Y. Deng, Y. Wu, Y. Bai, X. Zheng, J. Wang, Y. Fang, H. Wei, W. Ma, X. C. Zeng, X. Zhan and J. Huang, *Adv. Mater.*, 2017, **29**, 1604545.

S7 P. W. Liang, C. Y. Liao, C. C. Chueh, F. Zuo, S. T. Williams, X. K. Xin, J. Lin and A. K. Jen, *Adv. Mater.* 2014**, *26***, 3748.

S8 J. W. Jung, C.-C. Chueh and A. K. Y. Jen, *Adv. Energy Mater.* 2015**, *5***, 1500486.